Design and Development of a knee rehabilitation exoskeleton with four-bar linkage actuation

C. Y. Aubeeluck[1], S. Kölbl[1], D. Dobriborsci[1] and W. Aumer[1]

Abstract— In this paper, the design of a lower limb active exoskeleton for rehabilitation purposes is discussed. Active exoskeletons provide the additional required force for motion and gait correction, especially for patients who have suffered from limb impairment. The development was carried out taking into account sensor input for the control system. A Finite-State Machine (FSM) enables the different motions which rely on the data from the torque and acceleration sensors. To replicate the anatomical knee rotation, a four-bar linkage was modelled and integrated in the actuator drive. For this project, a prototype was created using Additive Manufacturing Processes (AMP). The prototype is part of the 'ForCEs' project at Deggendorf Institute of Technology (DIT) and was tested at an experimental stage for an initial set of results.

I. INTRODUCTION

A variety of conditions results in the impairment of the knee joint, namely chronic illnesses such as cerebral palsy and arthritis, for which the most common treatment is physiotherapy [1]. In modern physiotherapy, active exoskeletons, such as MINDWALKER [2], ReWalk [3], and HAL [4], are mechanized wearables that can be used to assist in rehabilitation. With the use of innovative actuating technologies, and novel material manufacturing processes, researchers have come up with exoskeletons that require the least assistance from medical experts. For rehabilitation, the 'MINDWALKER' uses a compact and compliant series elastic actuator with a Brushless DC motor (BLDC). However, despite BLDCs being the most popular actuation choice, bulkiness and low acceptability with patients remain an issue. Another feature is the intent detection for disabled patients. The 'ReWalk' exoskeleton consists of a remote control as its input, while the 'HAL' by Cyberdyne is the only assistance device with Electromyography (EMG) sensors. While the surface-EMG sensors' feasibility has been verified, there are still limitations such as noise due to poor adhesion. Furthermore, surface-EMG and EEG electrodes must be adhered to the patient for best results, which drastically decreases their practical usage for daily life applications. Table I summarizes the key elements of the state-of-the-art exoskeletons.

Exoskeleton	Sensing Method	Actuating Method	Joint Type
MINDWALKER	IMU	linear actuator	single-pivot
ReWalk	Tilt and Torque	dc motor	-
HAL	EMG	dc motor	single-pivot

TABLE I: State of the art exoskeletons (IMU: Inertial Measurement Unit).

[1]Deggendorf Institute of Technology, TC Cham, 21 Badstraße, 93413 Cham, Germany   chandra.aubeeluck@th-deg.de

Based on the review of exoskeletons' sensors, IMU's alone serve little purpose in intent detection as they cannot distinguish between the person's and the actuator's motion. However, if a secondary or more sensors' data are combined, an estimation can be obtained. In the ForCEs project [5], a combination of IMU's and torque sensor has been implemented. This reduces the inconvenience with surface-EMG electrodes. Furthermore, the resistance in motion can be monitored effectively, as opposed to an EMG only solution, where specific muscular activity has to be categorized. At the same time, an adaptive position is generated since the IMU and an angle sensor monitor the leg velocity changes.

By not using a single-pivot joint, the polycentric rotation of the knee, due to the roll and glide motion, has been replicated. One possibility to replicate the anatomical knee rotation is mentioned in [6], where a four-bar linkage approach is introduced. In our case, a similar mechanism has been devised which closer resembles the ligaments inside the knee. These are the Anterior and Posterior Cruciate Ligaments (ACL and PCL) [7]. The femur and tibia bones are the two additional links. The changing centre of rotation is demonstrated in Figure 1. Another key aspect is the use of AMP which improves the form, fit and function of the support structure and actuator. With a backdrivable speed reduction mechanism, the use of a clutch system is eliminated, which makes the actuator lighter.

After a short introduction, the limitations of existing designs are discussed in Section II. Afterwards, the modelling and design of proposed relevant solutions are explained in Section III. Next, in Section IV, an analysis of the implemented solutions is performed and discussed. At the end of Section IV, the obtained results are evaluated. A general emphasis is laid on the overall design concept including the control system, with particular attention to the actuator and four-bar linkage design.
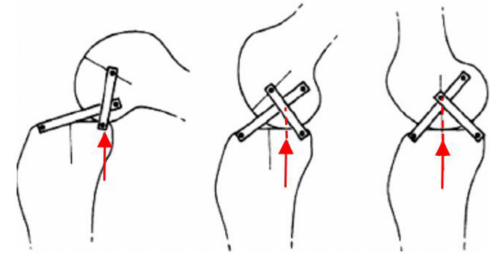

Fig. 1: Four-bar linkage in the knee. The shifting instantaneous centre of rotation (ICR) is indicated by the red arrow.

II. PROBLEM STATEMENT

The four-bar linkage provides a more adaptive rotation of the actuator joint, given the fact that the axis of rotation of the knee is not the same for every person. A proposed solution is aligning the ICR of the actuator and that of the knee by using parts made by AMP for lightweight supports that conform to the leg profile. An improved control algorithm with torque sensors and IMUs would overcome the current limitations and requirements with existing intent detection means. The extent to which this is resolved is discussed in this paper. While the four-bar linkage provides a more adapted solution, it also introduces the problem of irregular force output in which there is a reduction of up to 40 % of the input force. This is further described in [6]. By knowing the exact torque requirements for each angular position of the knee, the output torque can be adjusted, by varying the torque setpoint. While this is computationally not costly, it still requires an onboard online programming for the estimation of the output torque with respect to the input torques, and gait model torque. A lightweight control structure is thus desired, in which a complete modelling of the exoskeleton is simulated.

III. DESIGN OF CONTROL SYSTEM AND PROTOTYPE

The design for the complete exoskeleton was divided into four parts, namely the structural support, actuators, sensors, and the control system. Using the MSC Adams simulation software [8], a multibody simulation (MBS) at the musculoskeletal level was generated. To obtain the profile of the lower limbs in the sagittal plane, the Opti-Track System was used, where markers placed on the body gives the position of the upper and lower legs. From this, the support structure was developed in several stages starting with a simple element which was enhanced through topology-optimization.
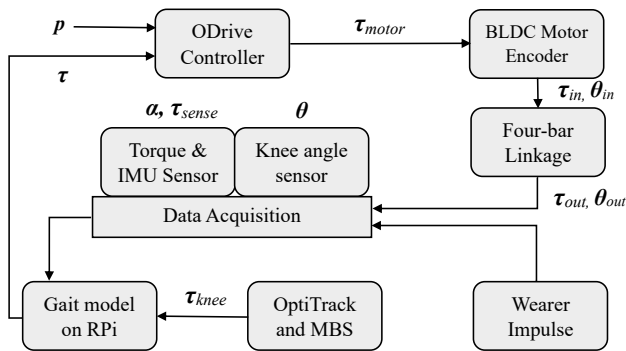
A. Control System Design

The components of the control system are illustrated in Figure 2, in which, τ is the torque, α is the tangential acceleration, and θ is the angle of the knee. Further torque variables are τ_{knee}, which is the knee required torque according to the gait model and τ_{sense}, which is sensed torque. In addition, τ_{motor} is the motor torque, τ_{in} is the four-bar linkage input torque at θ_{in} and τ_{out} is the output

Fig. 2: Representation of the exoskeleton Control System.

torque. The main input variable is designated as the position vector of the motor, p, which is the primary input to a proportional–integral–derivative (PID) controller, where the acceleration is related to the current or torque setpoint, I_d of the motor and the voltage V_{motor} varies the duty cycle, thus, the motor velocity $\dot{p}$. This is achieved through the ODrive BLDC Motor Controller [9].

B. Four-bar linkage mechanism

$L_1 = 17.43$
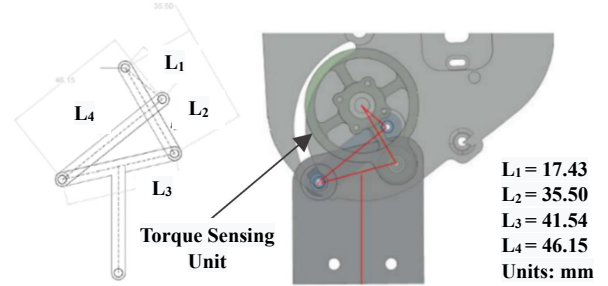$L_2 = 35.50$
$L_3 = 41.54$
$L_4 = 46.15$
Units: mm

Fig. 3: Four-bar linkage design: dimensions and integration.

The positions and the ratio of the lengths for the knee cruciate ligaments were taken based on the data from [10]. Breaking down the four-bar design, Figure 3 shows the obtained dimensions and design for the four-bar linkage integration. A free-body diagram (FBD) describes the forces in each link, including the relation between the input and output link. The base of the actuator serves as the fixed link L_1, which is offset by 40° to the horizontal. The variations in angular positions are determined by the Freudenstein Equations [11]. The angular range of motion for the input θ_{in}, defined by the input or crank link L_2, ranges from 20° to 90°. The output shank connects to link L_3 and its rotation θ_{out}, relative to the vertical, ranges from 0° to 110°. Link L_4 is referred to as the follower, as it determines the path of the output link L_3. Link L_2 is replaced by a torque sensing element, specifically designed to determine the effective torque input to the four-bar linkage. The forces are distributed in the four links, thus maximizing the permissible peak force acting the torque sensing element, as opposed to the torque sensing element directly transmitting the force to the shank link. In the Autodesk Inventor analysis, the forces are taken from the FBD of the four-bar linkage.
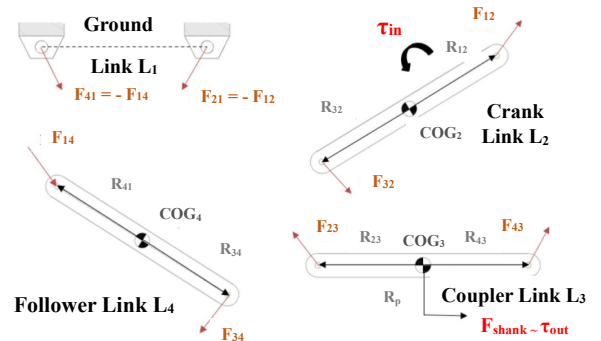

Fig. 4: FBD of four bars for single link analysis.

Figure 4 illustrates each link of the mechanism, clearly

showing the fixed Ground L_1 and the output force F_{shank} on the Link L_3. The vector quantities R_{ijxy} represent the distance from the Centre of Gravity (COG) and orientation of the links. From the FBD, the forces are resolved at static equilibrium to obtain Equation 1.

$$F_{out} = A^{-1} \cdot F_{in} \qquad (1)$$

where the 8th element of the (9×1) vector matrix F_{out} is the force acting on the shank, which is equivalent to the shank torque. Vector matrix F_{in} contains the elements of the input forces, which in this case is the input torque on the crank link L_2 as the 3rd element. The matrix A is represented in Equation 2. C is the shank length, which is 150 mm. As such, the input and output torques for the linkage are vectors which varies with the angular position. This relation is shown in Figure 5 as the actual torque output with respect to the knee angle.
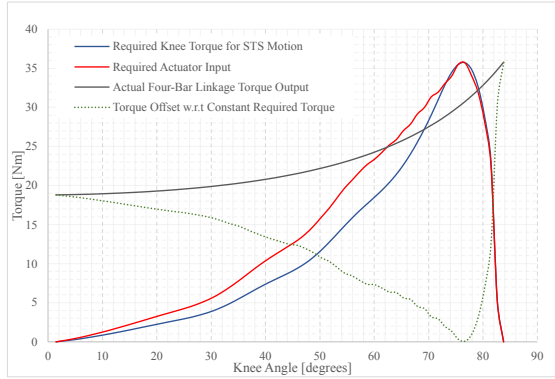

Fig. 5: Torque output from four-bar linkage and offset with respect to Sit-to-Stand (STS) Motion.

From Equation 2, a relation $\tau_{out} = g(\tau_{in}; \theta_{in})$ is obtained. By iterating the range of torque values with a resolution of 1 Nm, for each knee angle, a difference x exists, which is used in the computation of the actual motor input torque using Equation 3.

$$\tau_{motor} = \tau_{out} \times \left(\frac{1+x}{100}\right) \qquad (3)$$

where

$$x = \tau_{in} - \tau_{sense} \qquad (4)$$

Equation 4 and its parameters are explained further in section IV. The function $g(\tau_{in}; \theta_{in})$ is dependent on the Freudenstein calculation which is approximated by non-linear curve fitting to obtain

$$G(\theta_{in}) = -0.0064\theta^2_{in} + 2.01\theta_{in} - 37.15 \qquad (5)$$

The required output torque is mapped by the difference e between the output torque τ_{out} and the required torque for each gait τ_{knee} which varies with the angular positions of the knee. This is represented as the torque offset in Figure 5. The required knee torque τ_{knee} is part of the gait model which is represented by a dataset. For this project, the data is retrieved from a CSV file and are operated on as numpy arrays. This allows onboard computation to be performed

during the exoskeleton motion. With the required torque for each angular position known, the difference e is determined by first setting the input torque to the peak required torque. In this particular case, the peak required torque is 35 Nm and occurs at knee angle $\theta = 85^o$. The required actuator input τ_{motor} is determined using Equation 3. This is represented in Figure 5 as the required actuator input, where due to the four-bar linkage, in the range $20^o < \theta < 90^o$, the required actuator torque is decreased to the required knee torque to minimize the torque offset. Within that range, the required torque input is decreased by up to 53 % as shown by the torque offset curve.
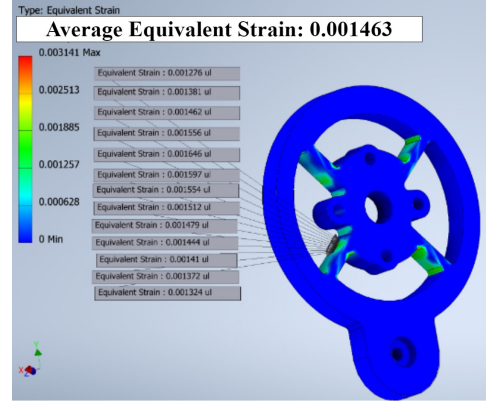

Fig. 6: FEA analysis on the torque sensing element.

For the torque sensing element, Aluminum 7075 alloy was chosen for its good elastic and yield strength properties. Figure 6 illustrates the Finite Element Analysis (FEA) on the torque sensing element, performed on Autodesk Inventor. Torque increments from 0 to 40 Nm were applied and for each increment, ε was the mean equivalent strain at the position indicated by the green-yellow region on the component. The thickness of that particular region is 2.5 mm and the maximum strain covers an area of 6 mm $\times$ 4 mm. An intersecting point where the least allowable safety factor of 2 was selected, and a linear relationship was developed with a slope m_s of 0.01214 Nm/ε and intercept K_s of $0.01Nm$.

C. Finite State Machine Control

Without registering any muscular activity, intent detection is only possible if the motor is backdrivable and not engaged. Given that the ForCEs exoskeleton is for rehabilitation purposes, it is designed to provide single motion bursts similar to an STS motion. Another type of motion is a swing or stance phase during a walking gait cycle, which last between 15% to 25% of a general walking gait. Thus, an FSM was generated to switch between motor rotation directions, and to switch between control modes of the ODrive controller. The FSM is illustrated in Figure 7. The initial motion detection occurs in state $'S0'$. States $'cw'$ and $'acw'$ correspond to clockwise (right side flexion) and anticlockwise (right side extension) respectively. If a counter motion is detected while in states $'cw'$ and $'acw'$, this sets the inputs states $'acw'_r$

$$A = \begin{bmatrix} 1 & 0 & 1 & 0 & 0 & 0 & 0 & 0 & 0 \\ 0 & 1 & 0 & 1 & 0 & 0 & 0 & 0 & 0 \\ -R_{12y} & R_{12y} & -R_{32y} & R_{32y} & 0 & 0 & 0 & 0 & 0 \\ 0 & 0 & -1 & 0 & 1 & 0 & 0 & 0 & cos(\theta) \\ 0 & 0 & 0 & -1 & 0 & 1 & 0 & 0 & sin(\theta) \\ 0 & 0 & R_{23y} & -R_{23y} & -R_{43y} & R_{43y} & 0 & 0 & C \\ 0 & 0 & 0 & 0 & -1 & 0 & 1 & 0 & 0 \\ 0 & 0 & 0 & 0 & 0 & -1 & 0 & 1 & 0 \\ 0 & 0 & 0 & 0 & R_{34y} & -R_{34y} & -R_{14y} & R_{14y} & 0 \end{bmatrix} \quad (2)$$
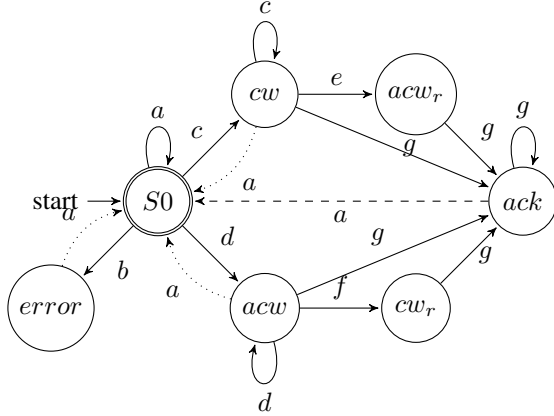

Fig. 7: FSM of the Control System.

and $'cw'_r$ correspondingly, denoting resistive motion. The exoskeleton control mode is switched between closed-loop filtered position control to closed loop torque control, to eventually an idle state, where the user's reaction is sensed before applying a further impulse, and repeating the cycle. For each state, the exoskeleton provides an assistive motion that corresponds to the direction registered, with a force proportional to the τ_{motor} torque. That motion is in the form of a linear ramp input to position p of the motor, with a time cycle of 70 ms. The thresholds for torque and acceleration detection are denoted as τ_t and α_t respectively. Input g relates to safety position limits reached, as well as a transition state after a resistive counter motion is detected. The main purpose is to serve as an acknowledgement state before a new intent is detected. The input for each state is detailed in Table II.

Inputs	IMU α	Torque τ_{sense}	Motor Torque τ_{motor}
a	$|\alpha| < \alpha_t$	$|\tau| < \tau_{t0}$	idle
b	$|\alpha| > \alpha_t$	$|\tau| < \tau_{t0}$	idle
c	$\alpha > \alpha_t$	$\tau < -\tau_{t1}$	idle
d	$\alpha < -\alpha_t$	$\tau > \tau_{t1}$	idle
e	$\alpha << -\alpha_t$	$\tau > \tau_{t2}$	$\tau_{motor} > \tau_{t1}$
f	$\alpha >> \alpha_t$	$\tau < -\tau_{t2}$	$\tau_{motor} < -\tau_{t1}$

TABLE II: Input parameters for the FSM.

IV. PROTOTYPE DEVELOPMENT AND EXPERIMENTS

After the design requirements were set and the required simulations performed, a prototype was developed. The three main aspects include the mechanical, electronics and software implementation. In this section, the experimental setups and results are discussed.

A. Setup of the control system

The main architecture comprises of a microcontroller with Analog-to-Digital (ADC) capability for data input, while the gait models were stored on a portable computer such as a Raspberry Pi (RPi), together with the Python scripts for computation. The main communication protocol for the sensor communications are an I²C bus. UART was used between the microcontroller and ODrive controller to transmit the motor position, although the RPi acts as a master node to eliminate time synchronization problem. The setup is illustrated in Figure 8 .
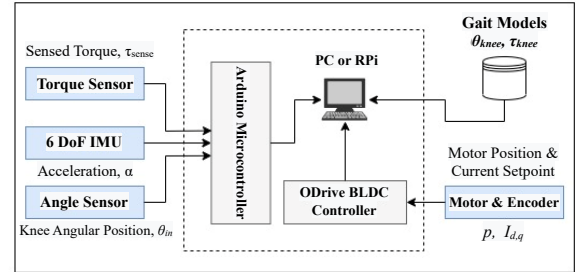

Fig. 8: Data capture interface.

The operation of the FSM is described by the torque and acceleration threshold parameters. Torque thresholds are denoted as vectors and consist of 3 levels – starting from the lowest being the backdrivable torque, the operation torque and resistive torque. In computational representation, the torque values are denoted as their analogue counterpart or voltage level of the sensors. To obtain the actual torque and current values, Equation 4 is further expanded into

$$x = (I_q \times K_T \times N) - (\frac{4 \times V_o}{S \times V_s} \times m_s) + K_s \quad (6)$$

where I_q is the motor current, K_T is the torque constant, N is the reduction ratio, S is the strain gauge factor, V_o is the strain voltage, which is equivalent to the torque sensing element voltage, and V_s is the bridge supply voltage. Two reduction ratios have been tested, namely 1:27 and 1:9, each with a BLDC of different torque constants. Furthermore, the third torque threshold is validated by the hall current sensors in the motor controller. From the simulation, the peak strain

on the Aluminum 7075 was 0.0016 (1600 $\mu\epsilon$). A $350\,\Omega$ linear strain gauge with gauge factor of 2 was used. Amplification was achieved with an INA125P instrumentation amplifier with a gain of 300. Torque and acceleration values were recorded for full flexion and extension motions, and are displayed in Figure 9. The torque values were determined using Equation 6. In comparison with the Table II, the input conditions are confirmed. Counter resistive torques occur at times $t = 1.6s$, $4s$ and $4.5s$. If the counter resistive torque is not accompanied by a sharp change in acceleration, the counter resistive motion is not registered. Similarly, the same case applies for sharp accelerations while torque values are within the peak thresholds. This occurs when the 'velocity gain' is lowered to allow a more compliant reaction. The threshold values τ_{t0}, τ_{t1} and τ_{t2} are $\pm 2.5\ Nm$, $\pm 5\ Nm$ and $\pm 15\ Nm$ respectively.
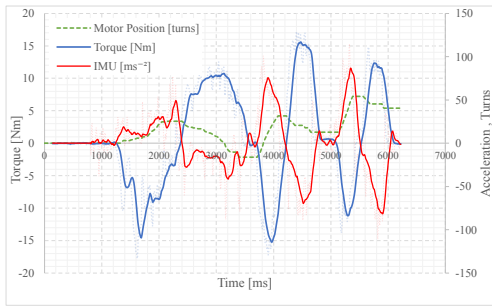

Fig. 9: Torque and IMU sensor values for intent detection.

The almost linear relation for the acceleration and torque parameters with respect to the knee angle are shown in Figure 10. In this particular case, the shank is accelerated to a constant speed of 60 deg/s. The slight variation of magnitudes less than 2 Nm is the result of the motor cogging torque which also contributes to the backdrivable torque. At a knee angle of 51°, this results in a shift in the two sensor readings, thus the importance torque-IMU sensor relation analysis.
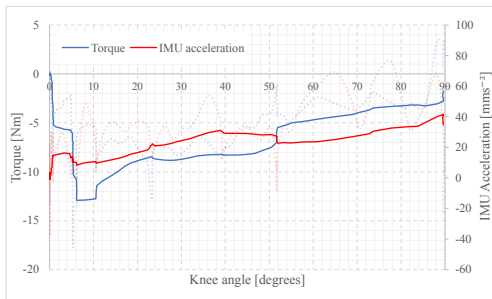

Fig. 10: Acceleration and Torque variation with knee angle.

B. Measurement of kinematic and kinetic parameters

A 6 Degree-of-Freedom (DoF) IMU was used as the measurement of the gyroscopic acceleration. It was placed at the length $C = 30\ mm$ from the link L_3 in the four-bar mechanism. Considering the knee angle θ, the knee angular acceleration is $\ddot{\theta}_{out} = \alpha \times C$. The thresholds were defined as a binary condition, but there is a direct relation between the

gyroscope acceleration and desired motion acceleration. The z-axis value was taken since the IMU sensor lies parallel with the limbs in the sagittal plane, thus only flexion and extension motions are recorded. The measurement of acceleration can be achieved by other devices, such as smartphones. It is further discussed in a separate paper part of the 'ForCEs' project [12]. An additional element is the 14-bit 'ams A5048' angle sensor, through which the position setpoint is confirmed and the angular velocity and acceleration at the crank input $L2$ of the four-bar is estimated. With onboard programming, the positions of the links are determined based on the angle sensor data and the Freudenstein function $G(\theta_{in})$ in Equation 5.

$$\theta_{out} = G(\theta_{in}) \tag{7}$$

C. Motion and Intensity Detection

To recognize a motion, the combination of the torque and IMU sensor was analyzed as shown in Table II. From Figure 9, the IMU values within $50\pm 10\ mm/s$ indicate a motion intent, which corresponds to the limits of motion with respect to the backdrivable torque. Acceleration values beyond $50\pm 10\ mms^{-1}$ indicate an instantaneous deceleration which only occurs when a resistive counter motion is performed. The motor position set point p, measured in $revolutions$ or $turns$, is equivalent to the knee angle through Equation 7. The difference between p_{is} and $p_{desired}$ is assigned as p_{offset}. With the relation $G(\theta_{in})$ known, the intensity of the acceleration $\ddot{\theta}_{out}$ was mapped linearly onto the p_{offset} value. The aim was to determine the motion within a time less than the general 300 ms human reaction time. With the latency in measurement being less than 100 ms, the actual delay t_d between a motion and a movement set point being generated was 70 ms, which is well below the 300 ms threshold.

D. Motor Control

The main tuning parameters reached are 'position gain' = 17 $(turn/s)/turn$, 'velocity gain' = 0.165 $Nm/(turn/s)$ and 'velocity integrator gain' = 0.32 $Nm/((turn/s) \times s))$. These correspond to their PID counterparts in the control structure. The 'CUI AMT-102' absolute encoder coupled to the motor provides incremental position feedback. Given the known time t_d, the relation in Equation 7 can be approximated to

$$p_{offset} \approx \frac{G^{-1}(\alpha) \times t_d^2 \times C}{N} \approx k \times G^{-1}(\alpha) \tag{8}$$

The set position p of the motor is represented in Figure 9. The plateau positions indicate a resistive counter motion where $p_{offset} = 0$. Motion is provided via torque bursts between the plateaus. A peak actuating speed of 360 deg/s and a peak torque of 30 Nm at full flexion was achieved for the actuator, which is 30% of the required knee torque for average pace walking [13].

E. Final actuator and structure design

The overall support structure consists of the hip and leg supports, which were 3D-printed with PA 2200 powder. FEA was used as a means of optimizing the form by analyzing

the compressive and tensile stresses along the surfaces of the exoskeleton structure. The peak axial and traverse forces that the structure can support are $0.7\ kN$ and $3.8\ kN$ respectively, while the peak moment about the joint is $80\ Nm$. The overall weight of each side of the exoskeleton is $1.57\ kg$. The completed prototype is illustrated in Figure 11. An STS motion is demonstrated as it successfully covers a full extension range of 0° to 100° of the actuator. The adjustable length of the upper leg caters for variable heights of people ranging from $1.7\ m$ to $1.85\ m$. A safety factor (SF) of 1.6 was achieved for the support limbs, while for the actuator, the SF was 2.
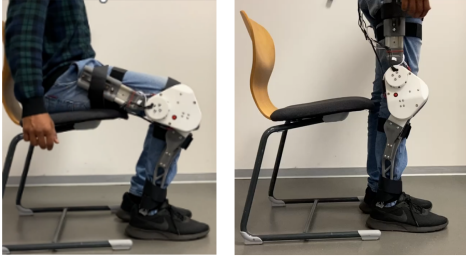

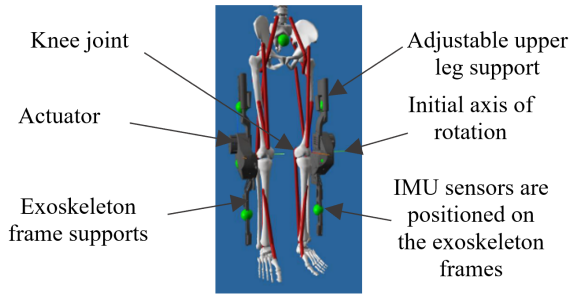Fig. 11: Exoskeleton prototype test with an STS motion.

Fig. 12: MSC Adams representation the musculoskeletal model and the exoskeleton, with axes alignment.

In Figure 12, a MBS taken from an OptiTrack Capture System is displayed. A CAD model of the actuator with four-bar linkage mechanism is included and a clear representation of the alignment of the exoskeleton with the profile of the leg can be observed. In the four-bar linkage, the ICR is determined by the cross-product links L_2 and L_3. In comparison with the knee model data from [6] and [14], the ICR follows the desired path. Since there is no feasible methodology to determine the precise ICR with respect to a fixed internal point, the initial ICR of the knee was estimated to be used as a reference point. This is represented as the initial axis of rotation at knee extension in Figure 12.

V. CONCLUSIONS

A prototype for the 'ForCEs' exoskeleton was developed that could serve the purpose of rehabilitation for patients with mild knee impairment. A unique design for the integration of the four-bar linkage which replicates the interior of the knee joint ligaments was proposed and assembled. This was tested successfully in both a simulation and on a prototype. Through topology optimization, an exoskeleton frame that could support direct forces up high compression axial forces and torques up to 30 Nm, was developed with additive manufacturing. Additionally, it provides a way to facilitate the development of personalized exoskeletons. The finite state algorithm operating with two sensors provide a new method of intent detection that does not rely on muscular activity which can be further improved with a trained AI model.

REFERENCES

[1] P. Lum, D. Reinkensmeyer, R. Mahoney, W. Z. Rymer, and C. Burgar, "Robotic devices for movement therapy after stroke: current status and challenges to clinical acceptance," *Topics in stroke rehabilitation*, vol. 8, no. 4, pp. 40–53, 2002.

[2] S. Wang, L. Wang, C. Meijneke, E. van Asseldonk, T. Hoellinger, G. Cheron, Y. Ivanenko, V. La Scaleia, F. Sylos-Labini, M. Molinari, F. Tamburella, I. Pisotta, F. Thorsteinsson, M. Ilzkovitz, J. Gancet, Y. Nevatia, R. Hauffe, F. Zanow, and H. van der Kooij, "Design and control of the mindwalker exoskeleton," *IEEE Transactions on Neural Systems and Rehabilitation Engineering*, vol. 23, no. 2, pp. 277–286, 2015.

[3] A. Esquenazi, M. Talaty, A. Packel, and M. Saulino, "The ReWalk powered exoskeleton to restore ambulatory function to individuals with thoracic-level motor-complete spinal cord injury," *American Journal of Physical Medicine &amp Rehabilitation*, vol. 91, no. 11, pp. 911–921, Nov. 2012.

[4] S. Ezaki, H. Kadone, S. Kubota, T. Abe, Y. Shimizu, C. K. Tan, K. Miura, Y. Hada, Y. Sankai, M. Koda, K. Suzuki, and M. Yamazaki, "Analysis of gait motion changes by intervention using robot suit hybrid assistive limb (HAL) in myelopathy patients after decompression surgery for ossification of posterior longitudinal ligament," *Frontiers in Neurorobotics*, vol. 15, Mar. 2021. [Online]. Available: https://doi.org/10.3389/fnbot.2021.650118

[5] C. Aubeeluck, "'forces' exoskeleton project," https://github.com/thd-research/ForCEs-Exoskeleton-Project, 2023.

[6] J.-H. Kim, M. Shim, D. H. Ahn, B. J. Son, S.-Y. Kim, D. Y. Kim, Y. S. Baek, and B.-K. Cho, "Design of a knee exoskeleton using foot pressure and knee torque sensors," *International Journal of Advanced Robotic Systems*, vol. 12, no. 8, p. 112, 2015.

[7] D. Saldias, D. Martins, C. de Mello Roesler, F. da Silva Rosa, and A. Ocampo Moré, "Modeling of human knee joint in sagittal plane considering elastic behavior of cruciate ligaments," in *22nd International Congress of Mechanical Engineering*, 2013.

[8] Hexagon, "Adams." [Online]. Available: https://hexagon.com/products/product-groups/computer-aided-engineering-software/adams

[9] O. Weigl, "Odrive." [Online]. Available: https://odriverobotics.com/

[10] F. D. Ruiz-Díaz, A. Altamirano-Altamirano, and G. Valentino-Orozco, "External knee prosthesis with four bar linkage mechanism," in *2016 13th International Conference on Electrical Engineering, Computing Science and Automatic Control (CCE)*. IEEE, 2016, pp. 1–6.

[11] F. Freudenstein, "An analytical approach to the design of four-link mechanisms," *Transactions of the American Society of Mechanical Engineers*, vol. 76, no. 3, pp. 483–489, 1954.

[12] S. Kirmess, C. Sigl, and W. Dorner, "Analysing movement patterns from smartphones for the training of exoskeletons," in *2022 12th International Conference on Advanced Computer Information Technologies (ACIT)*. IEEE, 2022, pp. 472–475.

[13] G. E. Caldwell, W. B. Adams III, and M. R. Whetstone, "Torque/velocity properties of human knee muscles: peak and angle-specific estimates," *Canadian journal of applied physiology*, vol. 18, no. 3, pp. 274–290, 1993.

[14] T. Besier, M. Schneider, N. Rooks, and M. Kazemi, "Model specifications abi–open knee data."